Journal of Materials Chemistry A

Accepted Manuscript

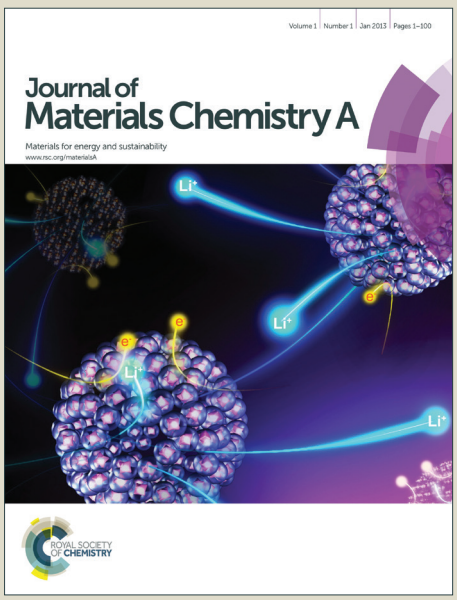

ROYAL SOCIETY OF CHEMISTRY

www.rsc.org/materialsA

Reduced graphene oxide nanosheets decorated with Au, Pd and Au-Pd bimetallic nanoparticles as highly efficient catalysts for electrochemical hydrogen generation

Gitashree Darabdhara[1,2], Mohammed A. Amin[3,4*], Gaber A.M. Mersal[3,5], Emad M. Ahmed[6,7], Manash R. Das[1,2*], Mohamed B. Zakaria,[8] Victor Malgras,[8] S. M. Alshehri,[9] Yusuke Yamauchi,[8,9] Sabine Szunerits[10] and Rabah Boukherroub[10*]

[1]*Materials Science Division, CSIR-North East Institute of Science and Technology, Jorhat 785006, Assam, India*

[2] Academy of Scientific and Innovative Research, Chennai–600113, India

[3]*Materials and Corrosion group, Department of Chemistry, Faculty of Science, Taif University, 888 Hawiya, Saudi Arabia*

[4]*Department of Chemistry, Faculty of Science, Ain Shams University, 11566 Abbassia, Cairo, Egypt*

[5]*Department of Chemistry, Faculty of Science, South Valley University, Qena, Egypt*

[6]*Materials and Corrosion group, Physics Department, Faculty of Science, Taif University, 888 Hawiya, Saudi Arabia*

[7]*Solid State Physics Department, National Research Center, Dokki, Giza 12311, Egypt*

[8] *National Institute for Materials Science (NIMS), 1-1 Namiki, Tsukuba, Ibaraki 305-0044, Japan*

[9] *Department of Chemistry, College of Science, King Saud University, Riyadh 11451, Saudi Arabia*

[10] *Institute of Electronics, Microelectronics and Nanotechnology (IEMN), UMR-CNRS 8520, University Lille 1, Avenue Poincaré – BP 60069, 59652 Villeneuve d'Ascq Cedex, France*

*Corresponding authors

maaismail@yahoo.com (MA Amin); Tel: +966(0)560480239

mnshrdas@yahoo.com (MR Das); rabah.boukherroub@iemn.univ-lille1.fr (R Boukherroub)

Abstract

Reduced graphene oxide (rGO) nanosheets decorated with gold nanoparticles (Au NPs/rGO), palladium nanoparticles (Pd NPs/rGO), and gold-palladium bimetallic nanoparticles (Au-Pd NPs)/rGO are synthesized by a simple solution chemistry approach using ascorbic acid as eco-friendly reducing agent. These materials are characterized by high resolution transmission electron microscopy (HRTEM), X-ray diffraction (XRD), X-ray photoelectron spectroscopy (XPS), and thermogravimetric analysis (TGA). The as-prepared nanocomposites are tested as electrocatalysts for efficient hydrogen evolution in deaerated 0.5 M H_2SO_4 aqueous solution using polarization and impedance measurements. Experimental findings show that the tested catalysts exhibit fast hydrogen evolution kinetics with onset potentials as low as −17, −7.2, and −0.8 mV *vs.* RHE for Au NPs/rGO, Pd NPs/rGO, and Au-Pd NPs/rGO, respectively. In addition, Tafel slopes of 39.2, 33.7 and 29.0 mV dec^{-1} and exchange current densities of 0.09, 0.11, and 0.47 mA cm^{-2} are measured for Au NPs/rGO, Pd NPs/rGO, and Au-Pd NPs/rGO, respectively. The tested materials not only maintain their high performance after 5000 sweep cycles, but their activity is simultaneously enhanced after this aging process. These findings reveal that the tested catalysts, particularly Au-Pd NPs/rGO, are promising candidates among other noble metal catalysts for hydrogen evolution, approaching the commercial Pt/C catalyst (onset potential: 0.0 mV, Tafel slope: 31 mV dec^{-1}, and exchange currrent density: 0.78 mA cm^{-2}). The high hydrogen evolution reaction (HER) activity of such materials is likely due to the abundance of active catalytic sites, the increased electrochemically accessible surface area and significantly improved electrochemical conductivity.

Keywords**:** Reduced graphene oxide nanosheets; Gold nanoparticles; Palladium nanoparticles; Gold-Palladium bimetallic nanoparticles; Electrocatalysis; Hydrogen evolution reaction.

1. Introduction

The ever increasing demand for energy accompanied with global warming and environmental deterioration has triggered the way towards utilization of hydrogen, often termed as a clean energy fuel carrier and referred to as "*fuel of the future*".[1, 2] High energy density, high efficiency and low pollutant emission are the prime factors for considering hydrogen as a future candidate for the replacement of fossil fuels. Thus, the production of hydrogen for clean energy applications has been a major area of focus.[3, 4] Due to their excellent catalytic activity and low corrosion resistance in acidic media, noble metal nanoparticles (NPs) are considered as the best hydrogen evolution reaction (HER) catalysts. Amongst effective HER electrocatalysts, Pt and its composites represent an important class for operations in acidic media due to their low reduction over potentials and fast reduction kinetics.[5] However, the high cost of Pt and its limited supply make the search for alternatives an important target. The focus has been shifted lately towards the use of electrode surfaces modified with NPs as efficient cathode materials for hydrogen generation.[6, 7] Recently, Pd was investigated as an alternative for Pt due to its high abundance and admirable catalytic activity. As such the use of Pd NPs was highly encouraged towards HER.[8, 9] However, as compared to Pt, Pd displayed less electrocatalytic performance towards HER. Thus, modification of the surface properties coupled with metal alloying are necessary to improve the electrocatalytic properties of Pd NPs.[10-13] In this context, attention may be shifted towards the use of alloyed NPs of Pd with other support that could bring changes in the electronic and geometrical properties of pure Pd.[11, 14]

For instance, bimetallic NPs comprising two different metal elements in the form of core-shell, alloy or heterostructures displayed enhanced chemical and physical properties and exhibited high catalytic/electrocatalytic properties. [15, 16] Through alloying Ag with Pd and subsequently modifying it with ionic liquid, Safavi *et al.* obtained improved electrocatalytic activity towards HER in comparison to pure Pd.[17] Likewise, alloying Pd with other noble and transition metals, active electrocatalysts

for HER were synthesized.[12, 14, 18, 19] Amongst bimetallic alloy systems, Au-Pd alloy is an ideal candidate for HER.[18, 19]

With the idea of improving the electrocatalytic activity of the electrocatalyst, loading the nanostructures on various carbon supports such as carbon nanotubes, carbon black or graphene has been suggested. Amongst different carbon supports, graphene and graphene oxide (GO) represents an excellent support for NPs synthesis, yielding graphene- and GO-based nanocomposites. Such nanocomposites have emerged as new star materials after the discovery of graphene,[20] and have been explored extensively for various applications, because of their extraordinary physical and chemical properties.[21-24] Theoretical calculations have shown that the interaction between metal and graphene would change the Fermi level of both the materials, playing an important role in enhancing the catalytic activity.[25, 26] Thus, it is of great interest to prepare graphene/GO-based metal NPs with excellent catalytic activity.

With the idea of substituting highly expensive Pt electrocatalyst, researchers have developed electrocatalysts based on 3D transition metals and other core-shell bimetallic nanostructures. Such nanostructures not only replace costly metals, but simultaneously act as efficient catalyst in several reactions. Ni-Pd core-shell NPs on multiwalled carbon nanotubes (MWCNTs) demonstrated excellent electrocatalytic activity in methanol oxidation.[27] The Au-Pd alloy system, as stated earlier, behaves as excellent electrocatalyst towards HER. Graphene nanosheets supported with Au-Pd bimetallic NPs is thought not only to improve the electrocatalytic properties of the alloy, but also to induce synergistic effects due to the excellent conductivity and high specific surface area of graphene.

Considering the importance of bimetallic alloyed graphene-based nanocomposite materials, we report in this paper the synthesis of Au, Pd and Au-Pd bimetallic NPs supported on reduced graphene oxide (rGO) matrix using a solution chemistry approach under mild reaction conditions. The as-synthesized nanocomposite materials were tested for the first time as electrocatalysts for the HER in 0.5 M H_2SO_4 aqueous solution, employing polarization and impedance studies. Stability of the best

catalyst was assessed employing repetitive cycling polarization and chronoamperometry measurements. The rGO-supported Au-Pd bimetallic NPs showed the highest performance, compared to Au NPs/rGO and Pd NPs/rGO, towards the HER. The Au-Pd NPs/rGO nanocomposite demonstrated its promising application as a stable catalyst for the HER, approaching the performance of commercial Pt/C; it exhibited an onset potential close to commercial Pt catalyst, a small Tafel slope of 29 mV per decade, an exchange current density of 0.47 mA cm^{-2} as well as no current loss after long-term chronoamperometry measurements.

2. Experimental

2.1. Chemicals and reagents

Graphite powder (<20μm, Sigma-Aldrich), sulfuric acid (AR grade, Qualigens, India), hydrochloric acid (AR grade, Qualigens, India), H_2O_2 (30%, Qualigens, India), potassium permanganate (>99 %, Merck, India), gold (III) chloride trihydrate (>99.9%, Sigma Aldrich), palladium (II) chloride (>99.9 %, Alfa Aesar), L-ascorbic acid (Sigma Aldrich) were supplied and used as received.

2.2. Preparation of graphene oxide (GO)

GO was synthesized from graphite powder adopting a modified Hummer and Offeman procedure.[28] Graphite oxide (1 g) was exfoliated in 100 mL of double distilled water using high power ultrasonicator for 3 h to obtain a reddish brown suspension of GO nanosheets at a concentration of 10 mg mL^{-1}.

2.3. Preparation of reduced graphene oxide (rGO)

rGO was synthesized from GO solution *via* reduction with ascorbic acid. Typically, GO suspension (2 mL, 10 mg/mL) was allowed to react with ascorbic acid solution (4 mL, 1 M) under stirring for 48 h at 25ºC to produce rGO nanosheets.

2.4. Synthesis of Au NPs/rGO nanocomposite

The as-obtained GO suspension (2 mL) was mixed with an aqueous $HAuCl_4$ solution (0.188 mL, 0.0212 M) and kept under stirring for 20 min after which ascorbic acid (4 mL, 1 M) was added. Finally, balanced amount of water was added to achieve a final reaction volume of 40 mL. The entire reaction mixture was stirred at 25°C for 48 h to produce rGO nanosheets decorated with Au NPs (Au NPs/rGO**)**.

2.5. Synthesis of Pd NPs/rGO nanocomposite

The as obtained GO suspension (2 mL) was mixed with an aqueous $PdCl_2$ solution (23.812 mL, 3 mM) and kept under stirring for 20 min after which ascorbic acid (4 mL, 1 M) was added. Finally, balanced amount of water was added to achieve a final reaction volume of 40 mL. The entire reaction mixture was stirred at 25°C for 48 h to produce rGO nanosheets decorated with Pd NPs (Pd NPs/rGO**)**.

2.6. Synthesis of Au-Pd NPs/rGO nanocomposite

For synthesis of Au-Pd NPs/rGO, 2 mL of GO suspension was mixed with an aqueous $HAuCl_4$ solution (0.188 mL, 0.0212 M) and $PdCl_2$ solution (23.812 mL, 3mM) and kept under stirring for 20 min after which ascorbic acid (4 mL, 1 M) was added. Finally, balanced amount of water was added to achieve a final reaction volume of 40 mL. The entire reaction mixture was stirred at 25°C for 48 h to produce rGO nanosheets decorated with bimetallic Au-Pd NPs (Au-Pd NPs/rGO**)**.

2.7. Characterization techniques

Transmission electron microscopy (TEM) images and elemental mapping images were recorded on a JEOL JEM-2011 electron microscope operated at an accelerating voltage of 200 kV.

X-ray diffraction (XRD) analysis was carried out using a Rigaku X-ray diffractometer (model: ULTIMA IV, Rigaku, Japan) with a scanning rate of 3 $deg \cdot min^{-1}$ from 5-100^o with a Cu Kα X-ray source (λ = 1.54056 Å) at a generator voltage of 40 kV and a generator current of 40 mA.

X-ray photoelectron spectroscopy (XPS) measurements were performed with an ESCALAB 220 XL spectrometer from Vacuum Generators featuring a monochromatic Al Kα X-ray source (1486.6 eV) and a spherical energy analyzer operated in the CAE (constant analyzer energy) mode (CAE = 100 eV for survey spectra and CAE = 40 eV for high-resolution spectra), using the electromagnetic lens mode. The angle between the incident X-rays and the analyzer is 58°. The detection angle of the photoelectrons is 30°.

Thermogravimetric analysis (TGA) of the samples was performed using Thermal Analyzer (Model: Netzsch STA 449F3) at a heating rate of 10°C/min in nitrogen atmosphere from 20 ºC to 1000 ºC.

Specific surface area of the samples was recorded *via* nitrogen gas adsorption at 77 K applying Brunauer-Emmett-Teller (BET) calculations using Autosorb-iQ Station 1 (Quantachrome, USA). The samples were degassed at 200 ºC for 3 h prior to performing the experiment.

2.8. Electrochemical measurements

The working electrodes employed were prepared by mixing 65 wt.% of the as-prepared catalysts (rGO, Au NPs/rGO, Pd NPs/rGO and Au-Pd NPs/rGO nanocomposites) and 35 wt.% paraffin wax. Paraffin wax was heated till melting and then mixed with the catalyst to produce a homogeneous paste. The resulting paste was packed into the end of a syringe (i.d.: 2 mm). External electrical contact was established by forcing a copper wire down the syringe. The prepared electrode was left for 24 h in air to allow its final homogenization to proceed prior to use. The surfaces of the resulting paste electrodes were smoothened with a weighing paper and rinsed carefully with distilled water.

Electrochemical measurements were performed in a conventional three-electrode electrochemical standard cell. A saturated calomel electrode (SCE) and Pt foil were used as the reference and counter electrodes, respectively. Potentials were measured *vs* SCE and are reported *vs* reversible hydrogen electrode (RHE). As references, the electrochemical performances of commercial Pt/C and bare rGO were also conducted. Measurements were conducted in a 200 mL volume cell at room temperature

(25 ± 0.2^{o}C) using a temperature-controlled water bath. The electrochemical cell was connected to an Autolab Potentiostat/Galvanostat (PGSTAT30) coupled to an Autolab frequency response analyzer (FRA) with FRA2 module connected to a personal computer.

The electrocatalytic activity of the prepared nanocomposites towards the HER was studied in a 0.5 M H_2SO_4 aqueous solution using linear potential sweep voltammetry and electrochemical impedance spectroscopy (EIS). This test solution was sparged with Ar gas for 30 min prior to use. Ar bubbling was stopped to prevent convection effects and the argon blanket was maintained over the solution throughout the experiment. The working electrode was then immediately immersed in the test solution that was kept stirred during the measurements to remove in situ-emerged H_2 bubbles.

Linear sweep voltammetry (LSV) curves were recorded by scanning the potential towards the negative direction, starting from the corrosion potential (E_{corr}) down to a potential of -2 V *vs* SCE at a scan rate of 5.0 mV s^{-1}. Impedance measurements were performed in the frequency range of 0.01 Hz - 100 kHz with an AC voltage amplitude of 5.0 mV. The impedance spectra were recorded in 0.5 M H_2SO_4 solution as a function of the cathodic overpotential. The experimental data were fitted to an appropriate equivalent circuit model using the complex nonlinear least-squares method.

Before polarization and impedance experiments, the open-circuit potential of the working electrode was measured as a function of time during 60 min, the time necessary to reach a quasi-stationary value. In all cases, at least three separate experiments were carried out for each run to ensure reproducibility of the results. The reproducibility of the linear sweep voltammetry and impedance experiments was good. However, it is important to point out that the various parameters obtained from these measurements are the mean values from the independent experiments performed. The mean value and standard deviation of the results were calculated and reported.

The long-term stability of the tested catalysts was assayed by means of chronoamperometry and cyclic voltammetry measurements. Chronoamperometry measurements were performed at a constant cathodic potential of –0.7 V *vs.* SCE in 0.5 M H_2SO_4 for 24 h. During the cyclic voltammetry meas-

urements, the potential was swept linearly from the starting potential (E_{corr}) into the cathodic direction at a scan rate of 5.0 mV s^{-1} till a cathodic potential of −2 V *vs* SCE, and then reversed with the same scan rate till the starting potential to form one complete cycle. The process of cycling was repeated 5000 times without withdrawing the electrode from the solution and without time delay.

3. Results and Discussion

3.1. Characterizations of Au NPs/rGO, Pd NPs/rGO and Au-Pd NPs/rGO nanocomposites

The morphology of Au NPs/rGO, Pd NPs/rGO and Au-Pd NPs/rGO nanocomposites was characterized using TEM and high resolution transmission electron microscopy (HRTEM). The TEM images along with particle size distribution curves suggested a formation of well-dispersed and crystalline NPs. The average particle sizes were (24 ± 0.716) nm for Au NPs and (13 ± 0.419) nm for Pd NPs (**Figure 1**). The lattice fringes with an interfringe distance of 0.23 nm corresponding to the (111) plane of face centred (*fcc*) Au NPs is shown in **Figure 1(c)**. Similarly, an interfringe distance of 0.19 nm corresponding to (200) plane of *fcc* Pd NPs is displayed in **Figure 1(e)**.

The TEM image of the Au-Pd NPs/rGO is displayed in **Figure 2a**; well-dispersed spherical Au-Pd NPs/rGO decorated the rGO nanosheets with a size distribution ranging from 25 to 35 nm. The average size calculated from the particle size distribution curve was found to be around (32 ± 0.375) nm (**Figure 2b**). The average size of the bimetallic Au-Pd NPs/rGO composites was slightly higher than that of their monometallic counterparts. The crystalline nature of the Au-Pd NPs/rGO nanocomposites was confirmed by selected-area electron diffraction (SAED) pattern and HRTEM. The lattice fringes assignable to (111) planes were clearly observed (**Figure 2c**). The NPs were highly crystalline in nature as evidenced by the SAED pattern. Therefore, the SAED patterns taken from 10,000 nm^2 (100 nm × 100 nm) exhibited several intense spots in random orientation, which can be assigned to -*fcc* crystalline structure. Furthermore, the Au-Pd/rGO nanocomposite was analyzed by high-angle annular diffraction field- scanning transmission electron microscopy (HAADF-STEM) technique

(**Figure 2B**). The elemental mapping of single NPs indicated a homogeneous distribution of Au NPs and Pd NPs; an indication of the formation of alloyed structure supported on the surface of rGO.

To further confirm that the bimetallic Au-Pd NPs exist as an alloy of the two metals rather than aggregated metal NPs, and to determine their crystal structure, wide-angle XRD measurements were performed on the bimetallic Au-Pd NPs/rGO (**Figure 3**). For comparison, **Figure 3** also includes the wide-angle XRD patterns of the individual monometallic Au NPs/rGO and Pd NPs/rGO nanocomposites. The XRD peaks of the three loaded NPs could be attributed to *fcc* structure. Distinct peaks of the monometallic Au NPs were seen at 2θ of 38.13°, 44.27°, 64.41°, 77.54° and 81.61° diffracted from the (111), (200), (220), (311) and (222) planes. For the monometallic Pd NPs, the peaks appeared at 2θ of 40.05°, 46.75°, 68.08°, 82.10° and 86.73° diffracted from the (111), (200), (220), (311) and (222) planes. For the bimetallic Au-Pd NPs, both crystalline phases of monometallic Au NPs and Pd NPs were visible at 2θ of 39.39°, 45.64°, 66.48°, 79.97 and 84.40°. It can be observed that each diffraction peak of the Au-Pd NPs/rGO composite was located between those of Au NPs/rGO and Pd NPs/rGO. In addition, compared with the standard diffraction patterns of Au, all the diffraction peaks of the Au-Pd NPs are slightly shifted to higher angles due to the substitution by Pd atoms. These findings indicated the formation of a single-phase alloy. Thus, Au-Pd NPs on rGO exist as an alloy and not as a mixture of monometallic NPs or core-shell NPs.

The average crystallite size, micro-strain and lattice constant were calculated from the XRD peaks and presented in **Table 1**. It was noticed that the lattice constant of Pd in the Au-Pd alloy enhanced from 3.958 nm (the lattice constant of the Pd element) to 3.968 nm, referring to expansion of the Pd unit cell due to the incorporation of Au atoms of larger atomic radius (0.144 nm) in the Pd crystalline lattice (atomic radius of Pd = 0.137 nm).[29] The incorporation of Au solute atoms resulted in a distortion of the crystal lattice, which in turn increased the micro-strain from 0.397% for Pd NPs to 0.492% for bimetallic Au-Pd NPs (**Table 1**). There is an acceptable agreement between the average size of the loaded monometallic and bimetallic NPs calculated from the particle size distribution

curves (**Figs. 1b, 1e and 2b**) and the average crystallite size (**Table 1**) deduced from the line broadening in the XRD spectra.

The XPS analysis on Au-Pd NPs/rGO was used to obtain information on the chemical composition of the composite materials (**Figure 4, Table 2**). For comparison, the spectra of Au NPs/rGO and Pd NPs/rGO prepared under identical conditions were included. The XPS survey spectrum of Au-Pd NPs/rGO showed peaks due to C_{1s} (284.4 eV), O_{1s} (532.6 eV), Au_{4f} (84.0 eV), and Pd_{3d} (337.6 eV). The Au_{4f} high resolution spectra displayed two peaks corresponding to $4f_{7/2}$ and $4f_{5/2}$ doublet at 84 and 87.6 eV, respectively (**Figure 4b**). The XPS binding energy of Au $4f_{7/2}$ was consistent with zerovalent Au. The high resolution XPS of Pd_{3d} revealed two doublets (**Figure 4c**). One pair at 335.6 and 340.9 eV corresponding to Pd $3d_{5/2}$ and Pd $3d_{3/2}$, respectively, in good agreement with the literature values (335.5 and 341.1 eV) of bulk Pd(0).[30] The other doublet at 338.3 and 343.6 eV is close to the reported values of Pd(II), suggesting that the Pd surface was partially oxidized.[31] Compared to monometallic Au(0) and Pd(0), shifts in binding energies of both Au_{4f} and Pd_{3d} towards lower binding energies are observed in Au-Pd NPs/rGO nanocomposite material. This observation is consistent with exchange of electrons between Au and Pd NPs. Moreover, due to incorporation of π electron rich rGO, it can be assumed that these electrons are transferred from the graphene to the metals.[32, 33]

Figure 5 depicts the C_{1s} high resolution spectra of the rGO matrix where Au, Pd and Au-Pd NPs were embedded. In the case of Au NPs/rGO composite, the C_{1s} spectrum can be deconvoluted into three components with binding energies at about 283.8, 285.7 and 287.9 eV assigned to C=C (sp^2 network), C-O and C=O species, respectively, with a C/O ratio of 6.4. The Pd NPs/rGO matrix can be deconvoluted into three bands: 283.8 eV (sp^2 network), 285.7 eV (C–O) and a band at 287.7 eV (C=O) with a C/O ratio of 5.2. The Au-Pd NPs/rGO nanocomposite showed two strong bands at 283.8 eV (sp^2 network) and 285.7 eV (C-O), together with smaller contributions at 286.2 eV (C–O–C) and 289.9 eV (COOH) with a C/O ratio of 3.08.[33] The strong band at 285.7 eV indicated the conversion of carbonyl and carboxyl groups into hydroxyl groups (C–OH) as ascorbic acid is a

mild reducing agent. The small contributions at 286.2 and 289.9 eV suggested the reduction of the epoxy and carboxylate functions of rGO. The spectrum of GO was added for comparison; it comprised three bands at 284.5 eV (C-C), 286.5 eV (C-O) and 287.9 eV (C=O).

The thermal stability of the composite material was depicted in the TGA (**Figure 6**). The weight losses in the TGA curves were seen at around 100 ºC, 200 ºC and above 600 ºC. The loss at around 100 ºC is attributed to the removal of water molecules trapped in between the graphene layers. Around 200 ºC, a 12.23% weight loss for Au-Pd NPs/rGO was observed due to reduction of oxygen containing functional groups like carboxyl, carbonyl, hydroxyl and epoxy. Another weight loss above 600ºC was due to the combustion of the carbon skeleton into CO and CO_2. The loss at 200ºC for Au-Pd NPs/rGO was comparable to that of the monometallic Au NPs/rGO and Pd NPs/rGO which were found to be of 12.35% and 14.43%, respectively. The TGA results clearly demonstrated the reduction of GO into rGO during the synthesis when compared with the TGA spectra of GO in literature.[34]

3.2. Catalytic hydrogen evolution

3.2.1. Linear sweep voltammetry (LSV) measurements

In order to demonstrate the HER electrocatalytic activity of such nanocomposite materials, cathodic polarization curves were constructed based on a LSV technique. The measurements were conducted in a 0.5 M H_2SO_4 aqueous solution, compared with a bare substrate (rGO nanosheets) (curve 1, **Figure 7**), at 25 ^oC and with a scan rate of 5.0 mV s^{-1}. A commercial Pt/C catalyst was also used as the standard (curve 5). The obtained cathodic polarization curves are shown in **Figure 7**: curves 2, 3 and 4 correspond to the Au NPs/rGO, Pd NPs/rGO, and Au-Pd NPs/rGO cathodes, respectively. It follows that the HER electrocatalytic activity of the rGO varied significantly according to the type and chemical composition of the NPs loaded on its surface. The bare rGO (curve 1) exhibited a minimal activity for H_2 evolution, as the proton reduction on its surface started at a highly negative po-

tential of E_c ~ -700 mV *vs.* RHE. Moreover, small cathodic currents were obtained for E_c < -700 mV. The electrode potential beyond which a sharp increase of the cathodic current is designated here as E_{HER}.

On the other hand, the reductive sweep curves of the three synthesized Au NPs/rGO, Pd NPs/rGO, and Au-Pd NPs/rGO nanocomposites (curves 2-4) exhibited a significant improvement in the HER activity. They showed, as clearly seen in the inset of **Figure 7**, low E_{HER} values of -17, -7.2, and -0.8 mV *vs.* RHE for the Au NPs/rGO, Pd NPs/rGO and Au-Pd NPs/rGO, respectively. Such lower over potentials gave rise to, as will be seen later on, higher cathodic currents and higher exchange current density values. This, in turn, favored hydrogen generation on their surfaces at lower over potentials, as compared with the literature.[19] These findings revealed at first sight that our three synthesized nanocomposites are active catalysts for the HER. Comparing the curves 2- to 4 revealed that the slope of the current density against the cathodic potential gets steeper, which reflects higher cathodic currents and increased kinetics for the HER. Thus, the HER electrocatalytic activity of the three catalysts is ranked following the sequence: Au NPs/rGO < Pd NPs/rGO < Au-Pd NPs/rGO. It seems therefore that the HER on the surface of rGO proceeds faster when the NPs of Au and Pd are brought together on the surface as bimetallic NPs (curve 4) than if they are loaded individually (curves 2 and 3). It is shown in the literature that bimetallic catalysts show superior catalytic properties *via* cooperative interactions (synergistic effects), which are not observable in their individual monometallic counterparts.[19, 35] These properties include higher electrocatalytic activity, better chemical/physical stability, greater surface area, and enhanced selectivity providing better catalytic performance. Based on these considerations, the high hydrogen evolution activity of our synthesized rGO-supported bimetallic Au-Pd NPs catalyst is likely due to the cooperativity effects among the NPs of Au and Pd, the increased number of active sites, and the increased electrochemically accessible surface area.

3.2.2. Analysis of polarization curves

The HER kinetics of the above catalysts was probed by the corresponding Tafel plots ($\eta_{H2/2H^+}$ *vs.* log *j*) and can be observed in **Figures 7b and 7c**. Linear portions of the Tafel plots were fitted to the Tafel equation {$\eta_{H2/2H^+} = \beta \log j + a$, where β (the Tafel slope) = ($2.3RT/\alpha F$) and a = ($2.3RT/\alpha F$) log j_o}, yielding the HER electrochemical kinetic parameters presented in Table 3. These parameters are the Tafel slope (β_c), and the onset potential of the HER (E_{HER}). The over potentials at an apparent cathodic current density of 1.0 mA cm^{-2} ($\eta_{1.0}$) and the current densities (j_o) at η = 0.0 V are also presented. The current density measured at η = 0.0 V defines the exchange current density (j_o), which represents the most important parameter describing the kinetics of the electrochemical charge-transfer reaction at specific metal/solution interface and is a measure of the electrocatalytic activity of various cathode materials towards the HER. All current densities were referred to the geometric area of the electrodes.

It follows from **Table 3** that the electrochemical kinetic parameters are significantly affected by the materials decorating the nanosheets of rGO. Tafel slopes of 39.2, 33.7, and 29 mV dec^{-1} were measured for Au NPs/rGO, Pd NPs/rGO, and Au-Pd NPs/rGO, respectively. By contrast, bare rGO exhibited inferior HER activity, as compared to our synthesized Au NPs/rGO, Pd NPs/rGO, and Au-Pd NPs/rGO nanocomposite catalysts, with a larger Tafel slope of 83.5 mV dec^{-1}. Compared to the Tafel slope measured for Pt/C catalyst (31 mV dec^{-1}), the Pd NPs/rGO catalyst presents a similar value (33.7 mV dec^{-1}), while the Au-Pd NPs/rGO catalyst (29 mV dec^{-1}) presents a lower, demonstrating the superior HER kinetics of these materials.

The HER inherent activity of these catalysts was also evaluated by j_o. Au-Pd NPs/rGO catalyst exhibits the highest j_o value (0.47 mA cm^{-2}) among the tested catalysts, namely Au NPs /rGO (0.085 mA cm^{-2}) and Pd NPs /rGO (0.11 mA cm^{-2}). It is more than 5 x 10^6 times larger than that recorded for the bare rGO (~8.9 x 10^{-8} mA cm^{-2}), and exceeded half that of Pt (0.78 mA cm^{-2}). The high electrode kinetic metrics (including onset potential of ~ -0.8 mV *vs* RHE, low Tafel slope of 29 mV dec^{-}

[1], and large j_o of 0.47 mA cm^{-2} highlight the exceptional H_2 evolution efficiency of the rGO-supported bimetallic Au-Pd NPs catalyst.

Further investigations of the HER electrochemical kinetic parameters presented in **Table 3** reveal that the over potentials at an apparent cathodic current density of 1.0 mA cm^{-2} ($\eta_{1.0}$) decrease significantly in comparison to that of the bare rGO (584 mV), facilitating hydrogen evolution on the surface of the materials at lower over potentials. For instance, the Au-Pd NPs/rGO catalyst exhibits the lowest $\eta_{1.0}$ value (~ 9.0 mV) among the tested catalysts ($\eta_{1.0}$ = 42 and 34 mV for Au NPs/rGO and Pd NPs/rGO catalysts, respectively), which is not much higher than that of Pt (~2.0 mV). These findings support the conclusion that the modification of rGO *via* the loading of Au NPs, Pd NPs, or bimetallic Au-Pd NPs on its surface enhances the HER kinetics significantly, with Au-Pd NPs/rGO catalyst being the most effective one.

3.2.3. Origin of catalytic activity

The high electrochemical activity of such catalysts towards the HER is most likely attributed to the strong chemical coupling between the rGO sheets and the loaded metal NPs. Such strong chemical interactions led to the selective growth of highly dispersed metal NPs (free of aggregation) on the rGO surface. The presence of these NPs on the rGO may afford abundant active catalytic sites for the HER. We hypothesize here that each supported metallic NPs can be considered as a "nanoelectrode" or even a "nanocathode" available for the reduction of protons.

The large electrochemical surface area of such catalysts may be another reason for their increased catalytic activity towards the HER. In addition, the surface area of the substrate itself may also play an important role in enhancing the electrochemical surface area of the catalyst as a whole. Indeed, the rGO nanosheets provide a large surface area for the good dispersion of the supported NPs, forming much smaller loaded NPs and thus, favoring the exposure of more active sites for the HER. BET measurements revealed that the specific surface area (S) of the bare rGO is significantly increased

from 0.735 m^2 g^{-1} to 58.799, 297.080, and 85.084 m^2 g^{-1} for Au NPs/rGO, Pd NPs/rGO, and Au-Pd NPs/rGO catalysts, respectively. This is the reason, in addition to the catalytic influence of the loaded NPs themselves, why our synthesized rGO-supported NPs exhibited superior electrocatalytic activity towards the HER compared with bare rGO. The small size of the Pd NPs loaded on rGO, together with the high *S* value (13 nm and 297.08 m^2 g^{-1}, respectively), may be the main reasons why the HER catalytic activity of such catalyst exceeded that of the Au NPs/rGO catalyst (24 nm and 58.799 m^2 g^{-1}, respectively). However, the bimetallic Au-Pd NPs/rGO catalyst (33 nm, 85.084 m^2 g^{-1}) exhibited the highest HER catalytic activity among the tested catalysts. These findings suggest that the cooperative catalytic influence between Au and Pd NPs in the loaded Au-Pd nano-alloy is the main reason behind the outstanding performance of the bimetallic Au-Pd NPs/rGO catalyst towards the HER.

It is generally known that the metal-support (M-S) interactions play an important role during catalysis.[36, 37] Strong M-S interactions accelerate the electron transfer from the support to the metal NPs, thus facilitating the reaction. Based on this, the improved HER catalytic activity of these materials can also be attributed to the strong electronic coupling between the loaded NPs and the rGO nanosheets. This in turn afforded rapid electron transport from the rGO sheets to the loaded metal NPs, thus contributing to the greatly enhanced catalytic activity toward the HER. To clarify this effect, EIS measurements were performed at a cathodic potential of -0.5 V *vs* SCE. From fitting the data (**Tables 4 and 5**), it can be observed that our catalysts exhibited significantly lower impedances than that of the bare rGO, confirming their high electrocatalytic activity towards the HER.

The complex-plane impedance plots of bare rGO and Pt (see the inset of **Figure 8**) displayed a capacitive loop related to the resistance capacitance (RC) network, consisting of the charge transfer resistance (R_{ct}) of H^+ reduction and the corresponding capacitance (C_{dl}) at the electrode-electrolyte interface.[38, 39] The capacitive loops of the rGO and Pt appeared as a single time constant in the corresponding Bode plots (not shown here). This impedance behavior was modeled by a simple electrical

equivalent circuit, presented in **Figure 9a**. On the other hand, two semicircles were observed for the three synthesized catalysts, as shown in the inset of **Figure 8**. The first one was observed at high frequencies with a diameter (resistance) R_1. The second one was noticed at medium- and low-frequency domains with resistance R_2. Such two time constants were quite clear in the corresponding Bode plots (not included here). The semicircle at high frequencies was attributed to the hydrogen adsorption, while the second one was assigned to the HER kinetics.[40] The impedance responses of the three catalysts tested can be modeled by the equivalent circuit presented in **Figure 9b**, where the overall impedance was characterized by a parallel combination of capacitance and resistance of two charge-transfer processes. The total charge-transfer resistance, R_{ct}, equals ($R_1 + R_2$). The circuit elements (Q_1 and R_1) and (Q_2 and R_2) were related to the high and the low frequency capacitive loops, respectively.[41] To describe this response properly, a constant phase element (CPE) was introduced in the equivalent circuit. The introduction of such a CPE was often used to interpret data for rough solid electrodes.[42] The impedance of the CPE, Z_{CPE}, is described by the expression:

$$Z_{CPE} = Q^{-1} (j\omega)^{-n} \quad (1)$$

where Q is the CPE constant (a proportionality factor), ω is the angular frequency (in rad s^{-1}), $j^2 = -1$, the imaginary number, and n is the CPE exponent. The values of the double-layer capacitances corresponding to the first and the second time constants (C_1 and C_2) can be calculated for a parallel circuit composed of a CPE (Q) and a resistor (R), according to the following formula:[43, 44]

$$Q = R^{-1}(RC)^n \quad (2)$$

The fitting parameters obtained for the tested materials were collected in **Tables 4** and **5**. From **Table 4**, the bimetallic Au-Pd NPs/rGO catalyst recorded the lowest charge-transfer resistance value (12.2 Ω cm^2), approaching that of the commercial Pt/C catalyst (9.1 Ω cm^2, **Table 5**) and extremely far from that of the bare rGO (25264 Ω cm^2, **Table 5**), among the tested catalysts (58.74 Ω cm^2 and 40.86 Ω cm^2 for Au NPs/rGO and Pd NPs/rGO, respectively). These findings supported Au-Pd NPs/rGO nanocomposite as an outstanding electrocatalyst for the HER. The significantly reduced

impedance afforded markedly faster HER kinetics with our synthesized catalysts. This was due to the fact that the metal NPs loaded on the rGO sheets behaved as free electroactive adsorption sites that enhanced the electron transfer in the system resulting in a lower semi-circle diameter, which means a decrease of the charge transfer resistance at electrode surface. **Table 4** also revealed that Au-Pd NPs/rGO catalyst had the largest capacitance (*Q* and *C*) value among all the tested catalysts. The large capacitance value of such catalyst corresponds to its large active surface area, as evidenced from BET measurements, which can highly promote its activity towards the HER.

Three possible reaction steps have been suggested for the HER in acidic media, including a primary discharge step (Volmer reaction):

$$H_3O^+ + e^- \rightarrow H_{ads} + H_2O, \text{ with } \beta = (2.3RT/\alpha F) \sim 120 \text{ mV} \quad (3)$$

where *R* is ideal gas constant, *T* is temperature, α~0.5 is the symmetry coefficient and *F* is Faraday constant. This is followed either by an electrochemical desorption step (Heyrovsky reaction):

$$H_{ads} + H_3O^+ + e^- \rightarrow H_2 + H_2O, \text{ with } \beta = \{2.3RT/(1+\alpha)\ F\} \sim 40 \text{ mV} \quad (4)$$

or a recombination step (Tafel reaction):

$$H_{ads} + H_{ads} \rightarrow H_2, \text{ with } \beta = (2.3RT/2F) \sim 30 \text{ mV} \quad (5)$$

The Tafel slope is the inherent property of a catalyst, and can be determined by the rate limiting step of the HER. The determination and interpretation of the Tafel slope are important to elucidate the elementary steps involved. With a very high H_{ads} coverage ($\theta_H \sim 1$), the HER on the Pt surface is known to proceed through a Volmer-Tafel mechanism (equations 3 and 5, respectively), and the recombination step is the rate limiting step at low over-potentials, as attested by the measured Tafel slope of 31 mV dec^{-1}.[45-48] The low Tafel slope of ~ 29 mV dec^{-1} measured for the Au-Pd NPs/rGO catalyst is the smallest ever measured with non-noble and noble metal HER catalysts, suggesting that the recombination step is the rate limiting step,[45-48] and the Volmer-Tafel mechanism is responsible for the HER catalysis.

3.2.4. Catalyst stability

The most important criterion for a good electrocatalyst is the durability. The best catalyst, namely the Au-Pd NPs/rGO is cycled continuously in 0.5 M H_2SO_4 solution at 25 ^oC at a scan rate of 5 mV s^{-1} for 5000 cycles. **Figure 10a** shows the LSV polarization curves of the Au-Pd NPs/rGO electrode after the 1st, the 3000th and the 5000th cycles. The polarization curves of the catalyst reveal only little changes after the 3000 and the 5000 cycles. It seems that the catalyst is activated upon cycling, as higher cathodic current densities were measured after the 3000th and the 5000th cycles. This activation enhances as the applied cathodic potential is made more negative, hydrogen evolving progressively. These findings indicate that the Au-Pd NPs/rGO catalyst not only possesses good long-term stability, but also activates during the operation. It is possible that, with repetitive cycling, the surface roughness increases (i.e., the ratio of true surface area to apparent surface area) due to which the surface area of the electrode increases progressively. Given the fact that Pd NPs is capable of absorbing hydrogen into its structure, the improvement of activity during stability testing might be due to pulverization of Pd NPs (i.e., an increase of surface area) due to hydrogen insertion-induced stress/stain.[49]

This phenomenon was highly reproducible. In addition, a preliminary experiment showed that the improved catalytic properties for the HER not only survive as long as the potential is kept at -2 V, where hydrogen evolves progressively, but also gets improved after some time. This means that the evolved hydrogen impacts on the catalytic effect. It may increase the surface area of the catalyst and creates new defect sites which are more favorable for the HER; a point of research that deserves further complementary study. However, before concluding on the beneficial role of hydrogen incorporation, one must make sure that another factor can be excluded, namely the deposition of Pt. Most often, Pt is used as the counter electrode (as it is the case here), and dissolution of minute amounts of Pt and its re-deposition at the cathode may be a more efficient mechanism responsible for improving

the catalytic properties. To exclude the possibility of Pt re-deposition, we made sure that the same improvements can be obtained when Au or carbon electrode are used as the anode instead of Pt.

To further clarify this effect, chronoamperometry measurements were carried out (**Figure 10b**). The current density of the Au-Pd NPs/rGO electrode decreased suddenly from -0.3 A cm^{-2} to -0.19 A cm^{-2} within the first 10 s of the run (catalyst deactivation, most probably due to catalyst poisoning and/or the detachment of some NPs from the substrate), then increased quickly over 24 h of continuous operation, exhibiting an increased catalytic activity for the HER. By comparison, under the exact same condition, the bare rGO exhibited similar features (as shown in the inset of **Figure 10b**): deactivation during the first 15 s of the run, followed by activation over the 24 h of continuous operation. This has occurred with much lower cathodic current densities as compared to the Au-Pd NPs/rGO catalyst. For instance, Au-Pd NPs/rGO recorded a cathodic current density of 0.34 A cm^{-2} after 24 h of continuous operation, which is 340 times greater than that measured for the bare rGO (~ 0.001 A cm^{-2}). This great difference in the cathodic current between the substrate itself and the catalyst is undoubtedly due to the catalytic influence induced by the loaded bimetallic Au-Pd NPs.

4. Conclusion

We reported a simple and green solution-phase synthetic approach for the synthesis of bimetallic Au-Pd NPs on rGO nanosheets using an eco-friendly reducing agent. The obtained Au-Pd NPs on the rGO nanosheets had an average size of (32 ± 0.375) nm. Via similar route, monometallic Au NPs/rGO and Pd NPs/rGO were also synthesized. The as-prepared nanocomposites were investigated as active electrocatalysts for efficient hydrogen evolution reaction in deaerated 0.5 M H_2SO_4 aqueous solutions using polarization and impedance measurements. An excellent electrocatalytic activity was observed for the bimetallic Au-Pd NPs/rGO catalyst, even after 5000 sweep cycles. Compared to the Au NPs/rGO and Pd NPs/rGO, the bimetallic Au-Pd NPs/rGO proved to be more promising among the noble metal hydrogen evolution catalysts, approaching the commercial Pt/C catalyst (onset potential: 0.0 mV, Tafel slope: 31 mV dec^{-1}, and exchange current density: 0.78 mA cm^{-2}). The activity of the bimetallic catalyst is attributed to the synergistic effect of Au, Pd and rGO. The present investigation might open up new possibilities towards the development of advanced materials to be used as potential electrocatalysts for different reactions.

Acknowledgment

The authors are thankful to the Department of Science and Technology, New Delhi for the financial support [SR/FT/CS-136/2011 (CSIR-NEIST Project title: GPP 269)] and Director, CSIR−NEIST, Jorhat for his interest to carry out the work. GD acknowledges DST, New Delhi, India for DST-INSPIRE Fellowship grant. RB and SS acknowledge financial support from the Centre National de la Recherche Scientifique (CNRS), the Lille1 University and the Nord Pas-de-Calais region. Y. Yamauchi extend his appreciation to the Deanship of Scientific Research support from the Visiting Professor Program of King Saud University to undertake Research in Saudi Arabia.

References

1 M. S. Dresselhaus and I. L. Thomas, *Nature*, 2001, **414**, 332−337.

2 J. A. Turner, *Science*, 1999, **285**, 687.

3 J. A Turner, *Science*, 2004, **305**, 972−974.

4 C. G. M. Guio, L.-A. Stern, and X. Hu, *Chem. Soc. Rev.*, 2014, **43**, 6555.

5 Z. Peng and H. Yang, *Nano Today*, 2009, **4**, 143.

6 T. M. Day, P. R. Unwin, and J. V. Macpherson, *Nano Lett.*, 2007, **7**, 51.

7 D. L. Feldheim, *Science*, 2007, **316**, 699.

8 F. Li, P. Bertoncello, I. Ciani, G. Mantovani, and P. R. Unwin, *Adv. Funct. Mater.*, 2008, **18**, 1685.

9 F. Li, I. Ciani, P. Bertoncello, P. R. Unwin, J. Zhao, C. R. Bradbury, and D. J. Fermin, *J. Phys. Chem. C*, 2008, **112**, 9686.

10 M. Shao, *J. Power Sources*, 2011, **196**, 2433.

11 P. J. Schafer and L. A. Kibler, *Phys. Chem. Chem. Phys.*, 2010, **12**, 15225.

12 F. A. Al-Odail, A. Anastasopoulos, and B. E. Hayden, *Top. Catal.* , 2011, **54**, 77.

13 L. A. Kibler, *Electrochim. Acta*, 2008, **53**, 6824.

14 M. Lukaszewski, T. Kedra, and A. Czerwinski, *Electrochim. Acta*, 2010, **55**, 1150.

15 D. S Wang and Y. D. Li, *Adv. Mater.*, 2011, **23**, 1044.

16 R. Ferrando, J. Jellinek, and R. L. Johnston, *Chem. Rev.* , 2008, **108**, 845.

17 A. Safavi, S. H. Kazemi, and H. Kazemi, *Fuel*, 2014, **118**, 156.

18 Z. Zhuang, F. Wang, R. Naidu, and Z. Chen, *J. Power Sources*, 2015, **291**, 132.

19 A. Abbaspour and F. Norouz-Sarvestani, *Int. J. Hydrog. Energy*, 2013, **38**, 1883.

20 K. S. Novoselov, A. K. Geim, S. V. Morozov, D. Jiang, Y. Zhang, S. V. Dubonos, I. V. Grigorieva, and A. A. Firsov, *Science* 2004, **306**, 666−669.

21 M. Liu, R. Zhang, and W. Chen, *Chem. Rev.*, 2014, **114**, 5117.

22 Y. Sun, Q. Wu, and G. Shi, *Energy Environ. Sci.*, 2011, **4**, 1113.

23 H. Chang and H. Wu, *Energy Environ. Sci.*, 2013, **6**, 3483.

24 X. Huang, X. Qi, F. Boey, and H. Zhang, *Chem. Soc. Rev.*, 2012, **41**, 666.

25 Q. J. Wang and J. G. Che, *Phys. Rev. Lett.*, 2009, **103**, 066802.

26 G. Giovannetti, P. Khomyakov, G. Brocks, V. Karpan, J. van den Brink, and P. Kelly, *Phys. Rev. Lett.*, 2008, **101**, 026803.

27 Y. C. Zhao, X. L. Yang, J. N. Tian, F. Y. Wang, and L. Zhan, *Int. J. Hydrogen Energy*, 2010, **35**, 3249.

28 W. S. Hummers and J. R. E. Offemann, *J. Am. Chem. Soc.*, 1958, **80**, 1339.

29 N. N. Greenwood and A. Earnshaw, *1997. Chemistry of the Elements (2nd ed.). Butterworth-Heinemann. ISBN 0080379419.*

30 S. Moussa, V. Abdelsayed, and M. Samy El-Shall, *Chem. Phys. Lett.*, 2011, **510**, 179.

31 A. R. Siamaki, A. El Rahman, S. Khder, V. Abdelsayed, M. S. El-Shall, and B. F. Gupton, *J. Catal.* , 2011, **279**, 1.

32 X. Chen, Z. Cai, X. Chen, and M. Oyama, *J. Mater. Chem. A*, 2014, **2**, 5668.

33 R. Wang, Z. Wu, C. Chen, Z. Qin, H. Zhu, G. Wang, H. Wang, C. Wu, W. Dong, W. Fana, and J. Wang, *Chem. Commun.* , 2013, **49**, 8250.

34 J.-N. Zheng, S.-S. Li, X. Ma, F.-Yi Chen, A.-J. Wang, J.-R. Chen, and J.-J. Feng, *J. Power Sources*, 2014, **262**, 270.

35 H. J. Sinfelt, *Acc. Chem. Res.*, 1987, **20**, 134.

36 G. C. Bond and D. T. Thompson, *Catal. Rev. Sci. Eng.*, 1999, **41**, 319.

37 M. Haruta, *Catal. Today*, 1997, **36**, 153.

38 J. Kubisztal, A. Budniok, and A. Lasia, *Int. J. Hydrog. Energy*, 2007, **32**, 1211.

39 I. Danaee and S. Noori, *Int. J. Hydrog. Energy*, 2011, **36**, 12102.

40 Y. Li, H. Wang, L. Xie, Y. Liang, G. Hong, and H. Dai, *J. Am. Chem. Soc.*, 2011, **133**, 72.

41 J. O'M. Bockris and E. C. Potter, *J. Electrochem. Soc.*, 1952, **99**, 169.

42 J. G. N. Thomas, *Trans. Faraday Soc.*, 1961, **57**, 1603.

43 B. E. Conway and B. V. Tilak, *Electrochim. Acta,* , 2002, **47**, 3571.

44 C. Gabrielli, P. P. Grand, A. Lasia, and H. Perrot, *J. Electrochem. Soc.*, 2004, **151**, A1943.

45 S. Martinez, M. Metikos-Hukovic, and L. Valek, *J. Mol. Catal. A*, 2006, **245**, 114.

46 J. R. Macdonald, 'Impedance spectroscopy', Wiley, New York, 1987.

47 X. Wu, H. Ma, S. Chen, Z. Xu, and A. Sui, *J. Electrochem. Soc.*, 1999, **146**, 1847.

48 H. Ma, S. Chen, B. Yin, S. Zhao, and X. Liu, *Corr. Sci.*, 2003, **45**, 867.

49 M. Lischka and A. Groß, 'Hydrogen on palladium: A model system for the interaction of atoms and molecules with metal surfaces', ed. Jarek Dąbrowski, Recent Developments in Vacuum Science and Technology, 2003: 111-132 ISBN: 81-7736-118-X, and references therein.

Table 1: Average lattice parameter, crystallite size and micro-strain of Pd NPs, Au NPs and Au-Pd NPs, calculated from XRD line broadening using the Debye Scherrer equation.

Matrix	lattice parameter (nm)	crystallite size, (nm)	micro-strain%
Pd NPs	0.389 (0.389)*	22	0.397
Au NPs	0.409 (0.407)**	42	0.196
Au-Pd NPs	0.393	28	0.492

* and ** refer to the lattice parameter of the corresponding bulk elements.

Table 2: Atomic percentage of different elements in the nanocomposites

Matrix	C_{1s}	O_{1s}	Au_{4f}	Pd_{3p}
Au NPs/rGO	86.26	13.47	0.26	-
Pd NPs/rGO	82.37	17.16	-	0.47
Au-Pd NPs/rGO	74.44	24.20	0.34	1.12

Table 3 - Mean value (standard deviation) of the electrochemical kinetic parameters for the HER on the surfaces of Au NPs/rGO, Pd NPs/rGO, and Au-Pd NPs/rGO catalysts in 0.5 M H_2SO_4 solutions, in comparison with those parameters recorded for bare rGO and Pt/C at 25 ^oC.

Catalyst	Onset potential (E_{HER}, mV *vs.* RHE)	Tafel slope (mV dec^{-1})	Exchange current density (j_o, mA cm^{-2})	Over potential at j = 1.0 mA cm^{-2} ($\eta_{1.0}$, mV)
bare rGO	-700(12)	83.5(1.7)	8.9(0.4) x 10^{-8}	584(5.4)
Au NPs/rGO	-17(0.9)	39.2(1.1)	0.085(0.004)	42(1.8)
Pd NPs/rGO	-7.2(0.3)	33.7(0.9)	0.11(0.007)	34(1.4)
Au-Pd NPs/rGO	-0.8(0.1)	29(0.5)	0.47(0.02)	9(0.4)
Pt/C	0.0(0.05)	31(0.2)	0.78(0.012)	2(0.1)

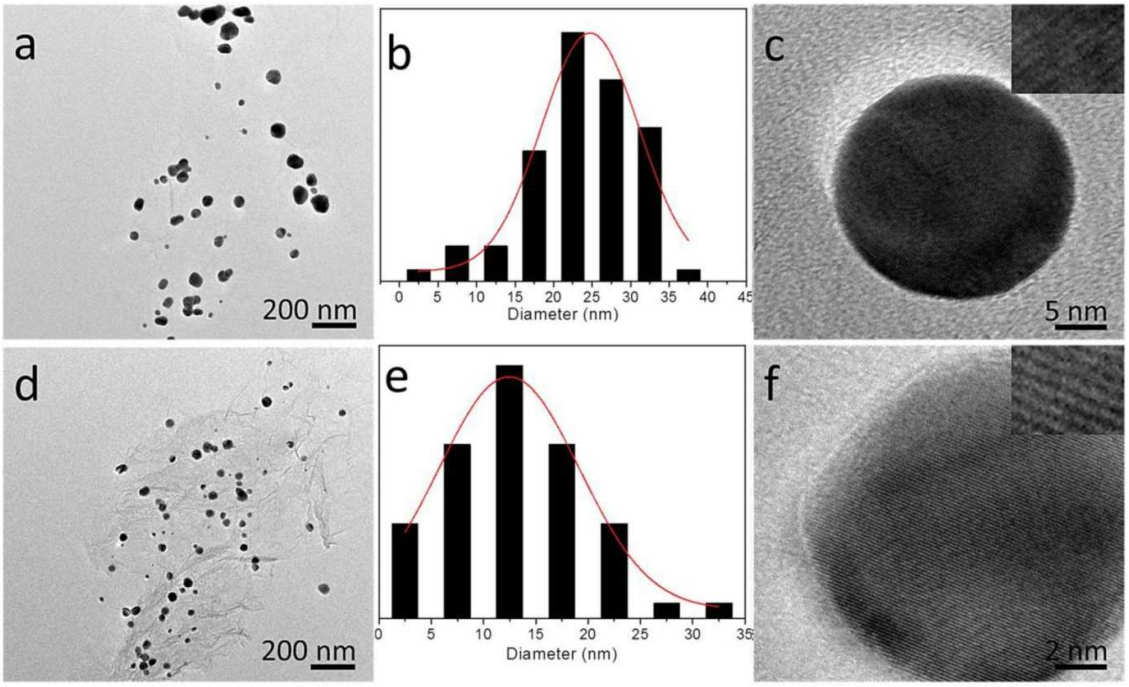

Figure 1: TEM study of (a-c) Au NPs/rGO and (d-f) Pd NPs/rGO.(a, d) Low-magnified TEM images of NPs on rGO, (b, e) the particle size distribution curves, and (c) high-magnified TEM image of a single NP. Lattice fringes for (111) fcc plane of Au NPs/rGO [Inset (c)] and (111) plane of fccPd NPs/rGO [Inset (f)] are clearly observed inside the particle.

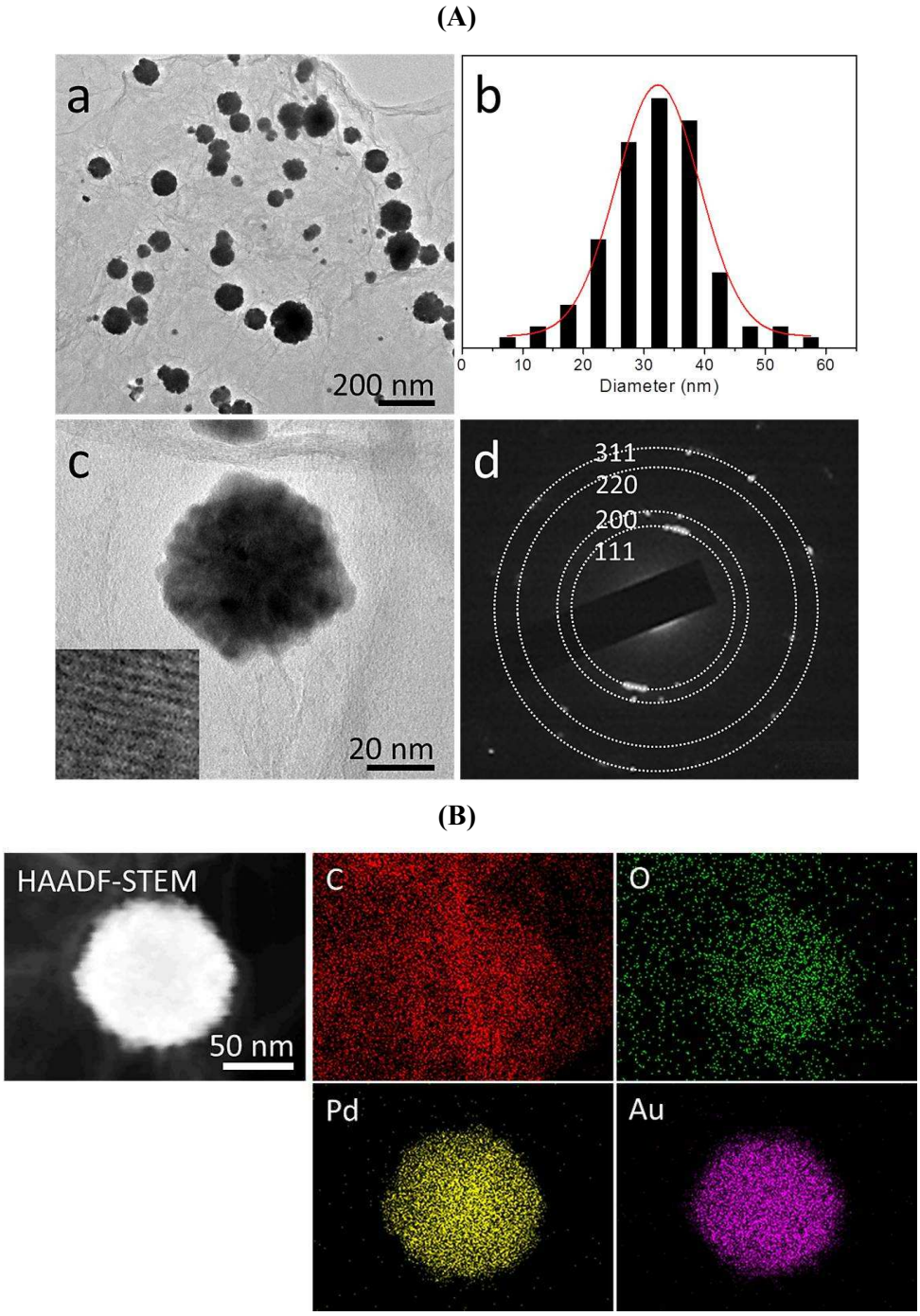

Figure 2: (A) (a) Low-magnified TEM image of bimetallic Au-Pd NPs/rGO, (b) the particle size distribution curve, (c) high-magnified TEM image of a single bimetallic Au-Pd NPs/rGO, and (d) selected-area electron diffraction (SAED) pattern. Lattice fringes are clearly observed inside the particle for (111) plane of Au-Pd NPs/rGO; (B) Elemental mapping of bimetallic Au-Pd NPs/rGO.

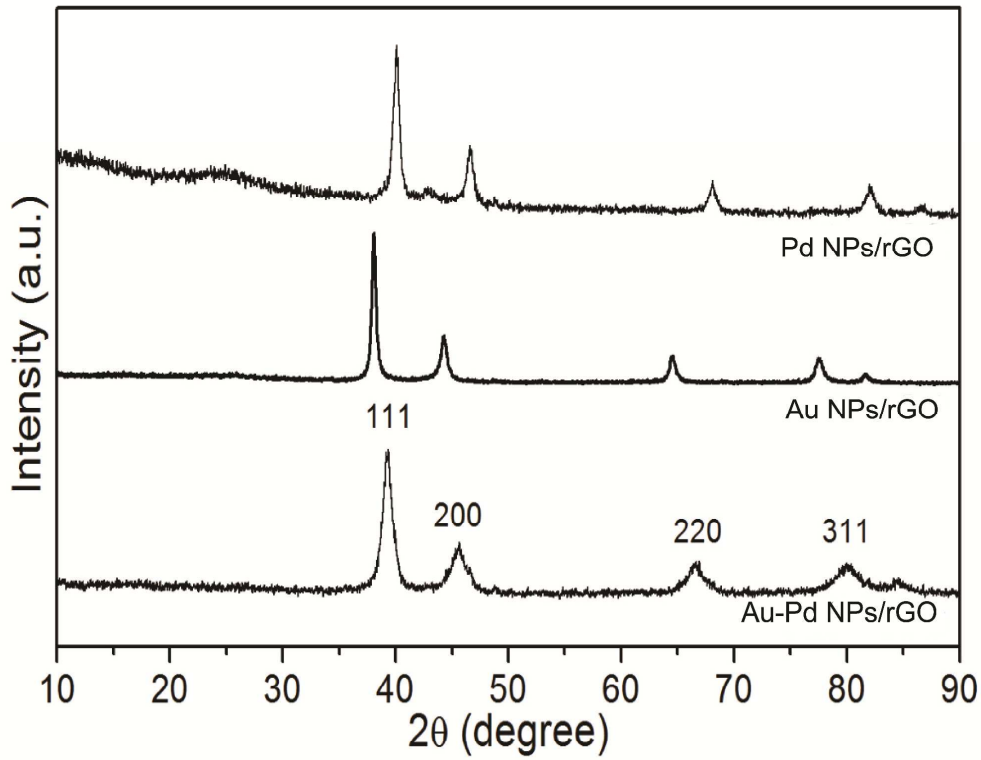

Figure 3: Wide-angle XRD patterns of Pd NPs/rGO, Au NPs/rGO and Au-Pd NPs/rGO nanocomposites.

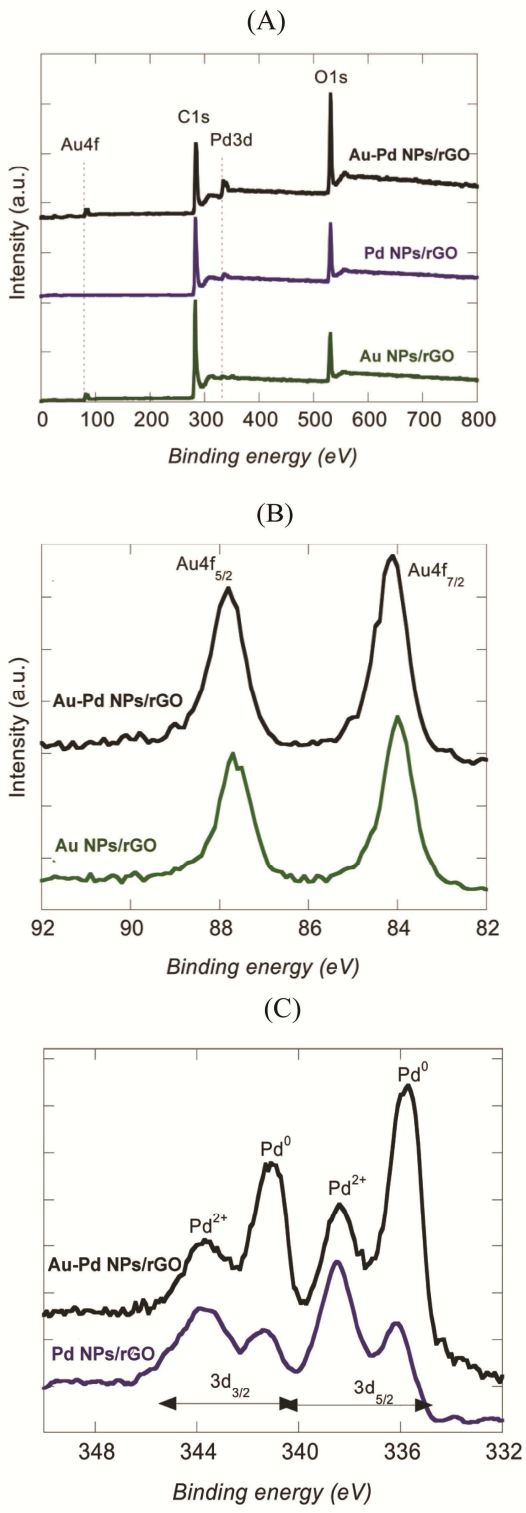

Figure 4: (A) XPS survey spectra of Au NPs/rGO (green), Pd NPs/rGO (blue) and Au-Pd NPs/rGO (black); (B) Au_{4f} high resolution XPS spectra of Au NPs/rGO (green) and Au-Pd NPs/rGO (black); (C) Pd_{3d} high resolution XPS spectra of Pd NPs/rGO (blue) and Au-Pd NPs/rGO (black).

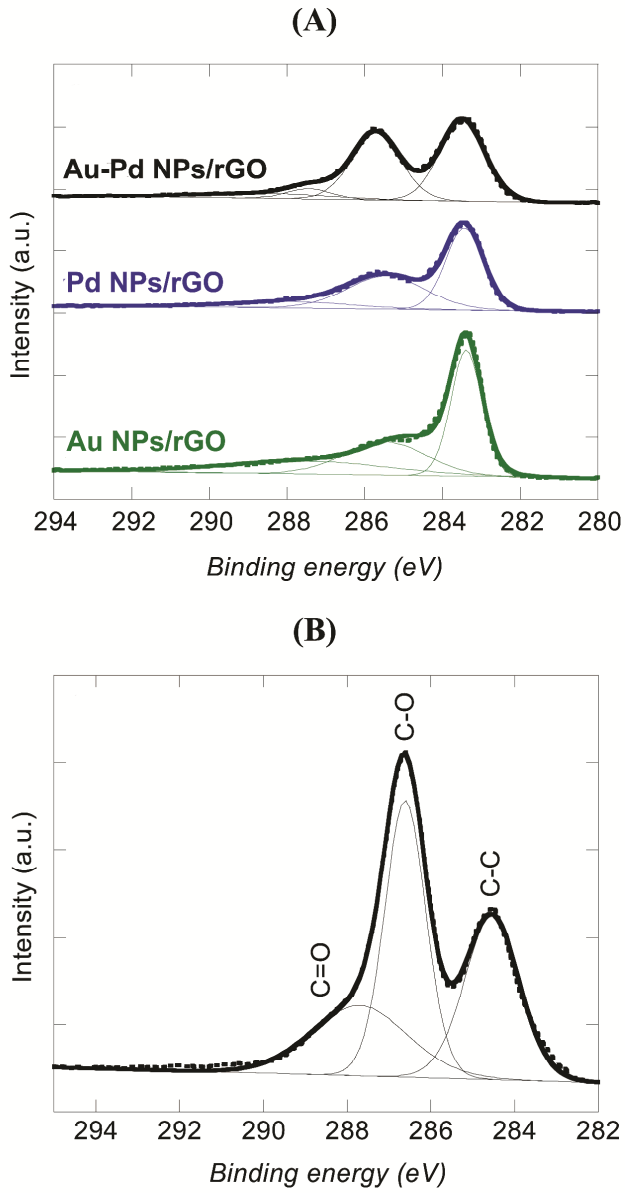

Figure 5: (A) C_{1s} high resolution XPS spectra of rGO nanosheets in Au NPs/rGO (green), Pd NPs/rGO (blue) and Au-Pd NPs/rGO (black); (B) C_{1s} of GO.

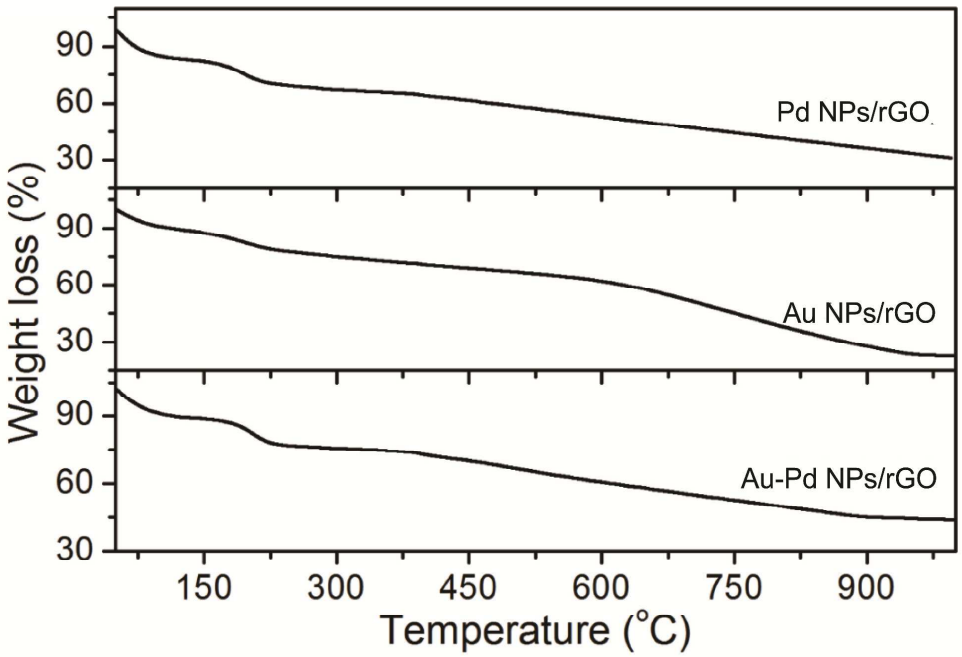

Figure 6: TGA curves of Pd NPs/rGO, Au NPs/rGO and Au-Pd NPs/rGO nanocomposites.

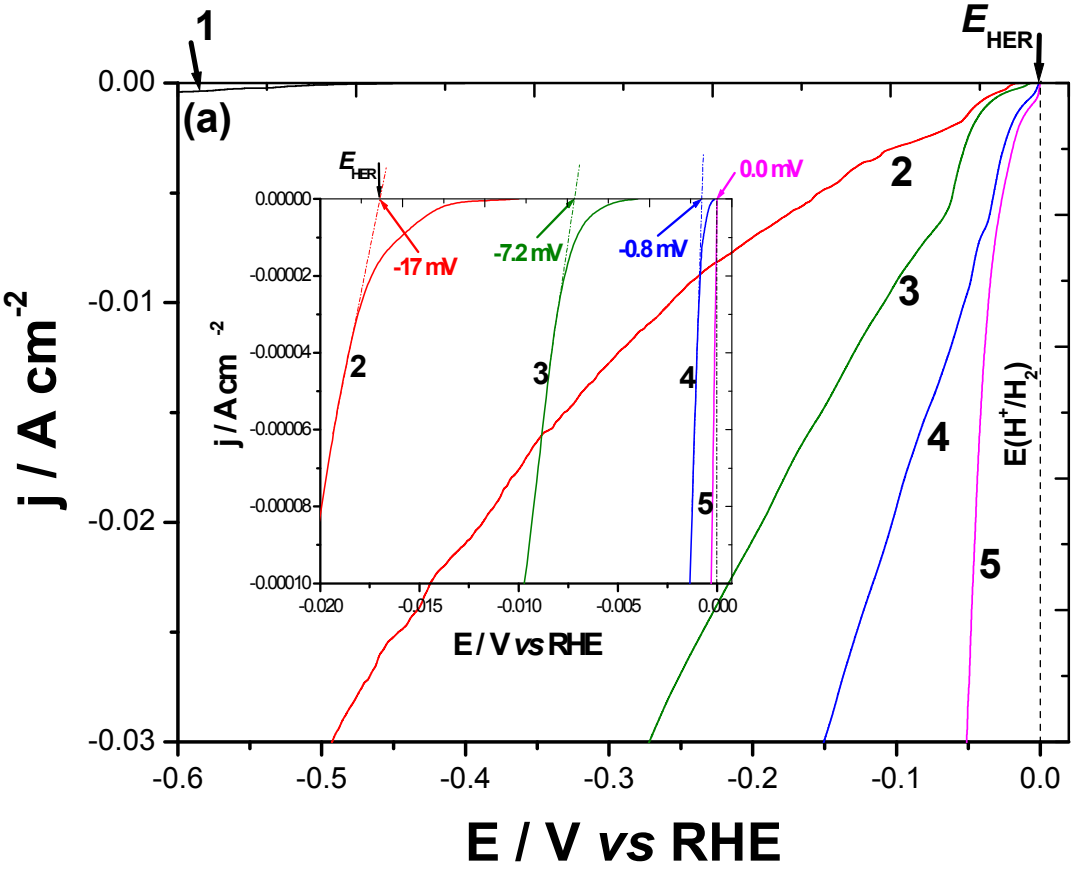

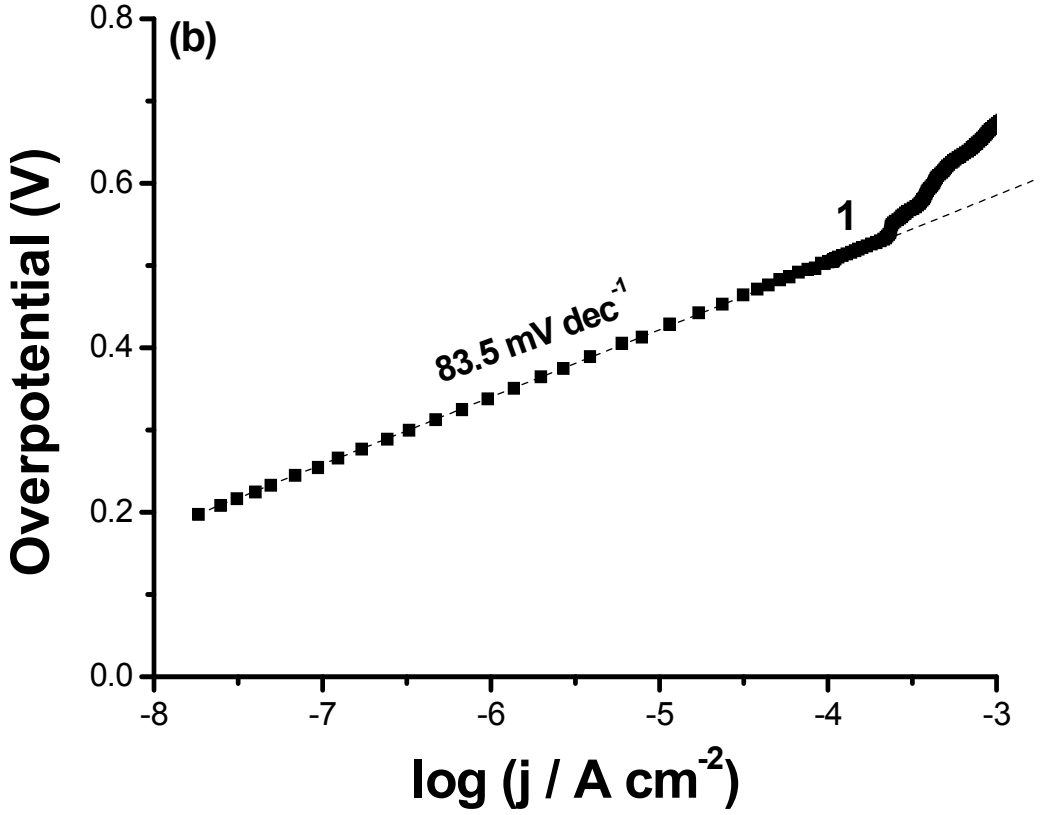

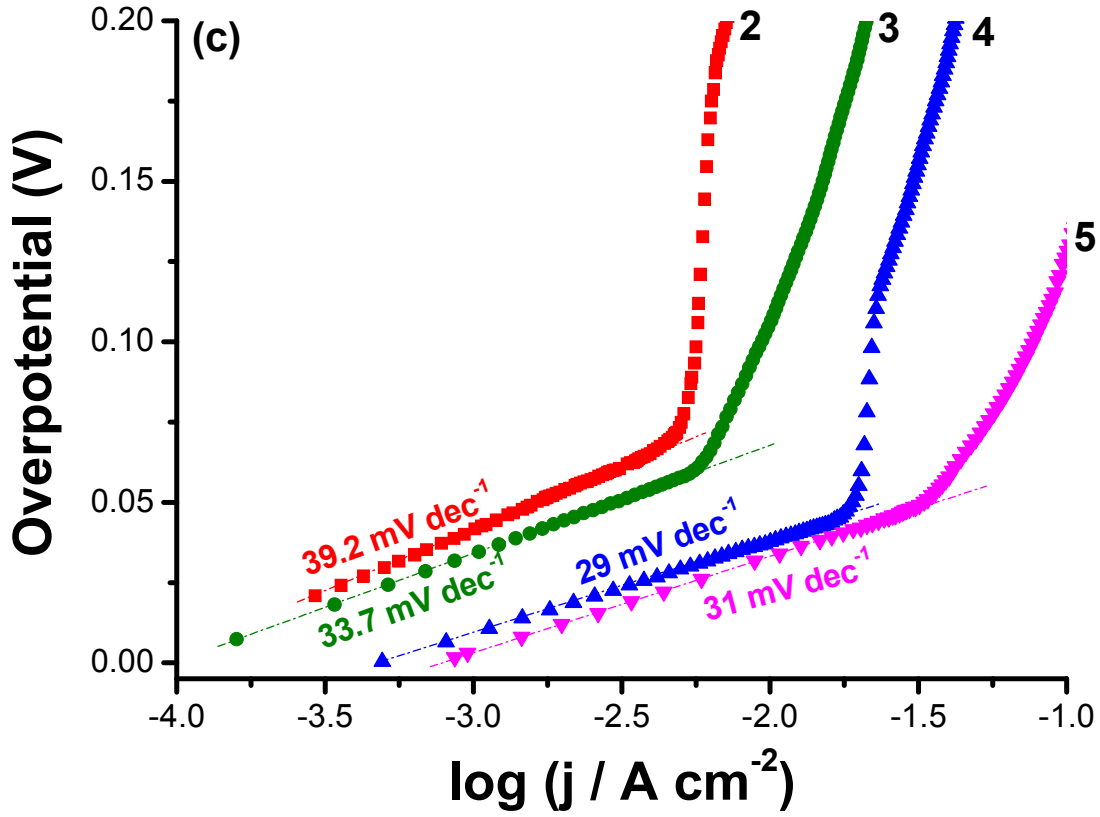

Figure 7: Electrocatalytic hydrogen evolution of different catalysts: **(a)** Polarization curves for the HER on (1) bare rGO, (2) Au NPs/rGO, (3) Pd NPs/rGO, (4) Au-Pd NPs/rGO, and (5) a commercial Pt/C catalyst. Measurements were conducted in deaerated H_2SO_4 aqueous solutions (0.5 M) at a scan rate of 5 mV s^{-1} at 25 ^{o}C. **(b and c)** Tafel plots for the tested catalysts derived from **(a)**.

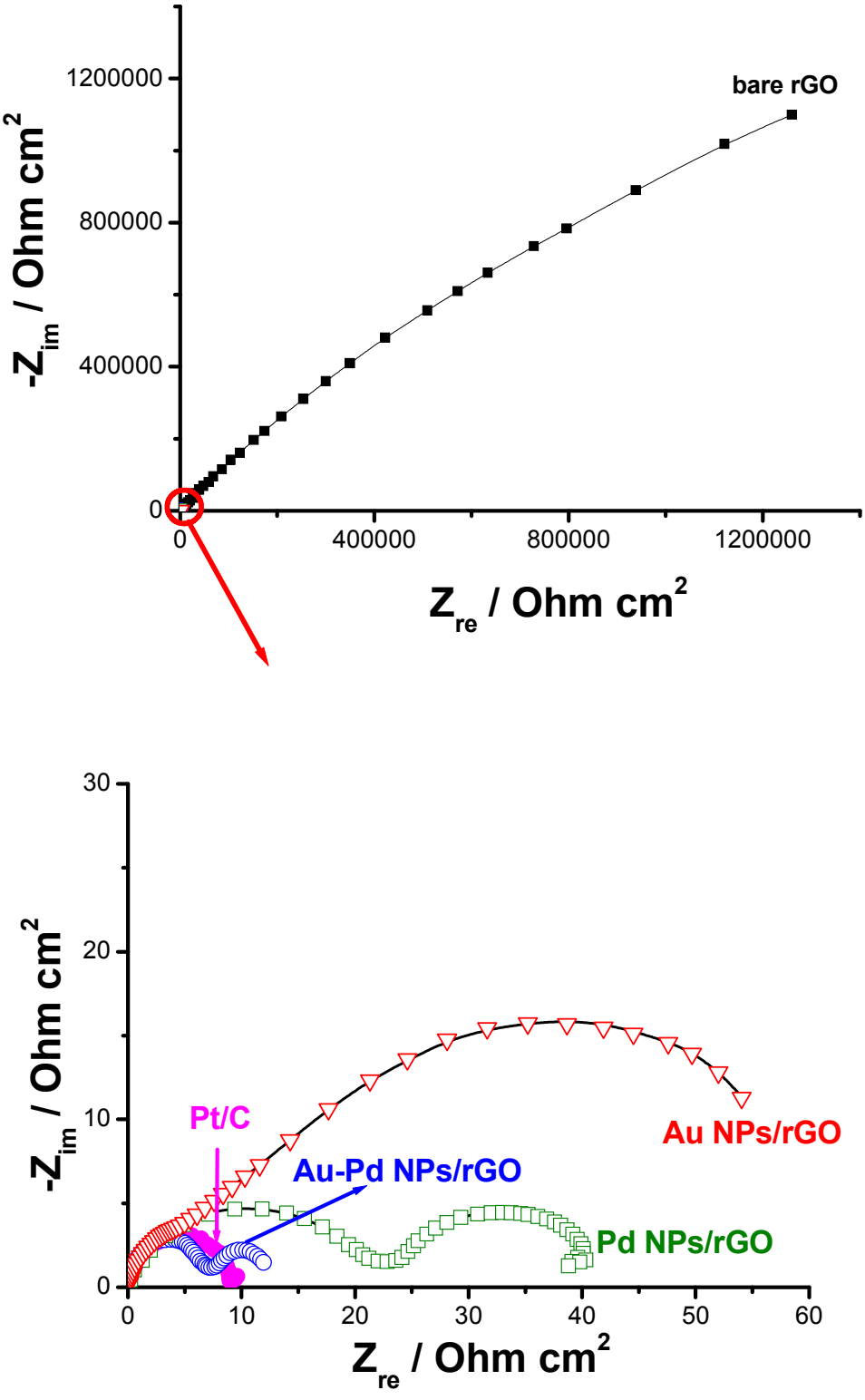

Figure 8: Complex-plane impedance plots recorded for the tested materials at a cathodic potential of -0.5 V *vs* SCE at 25 °C.

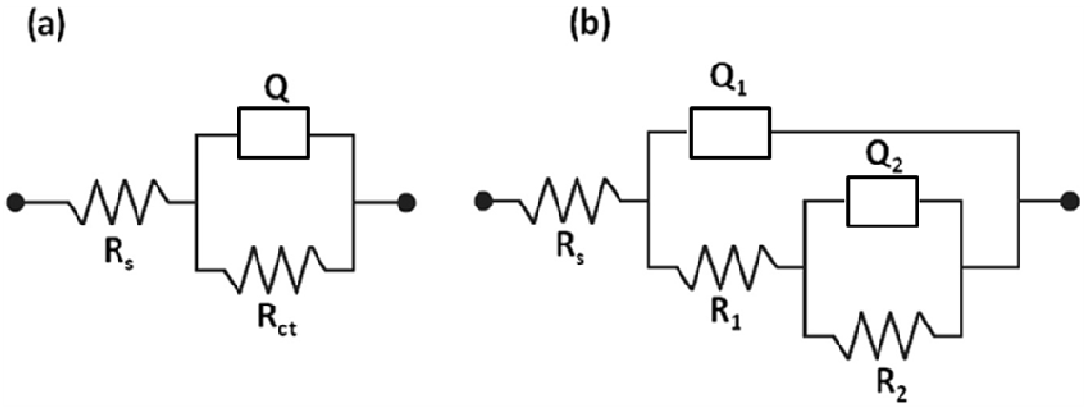

Figure 9: Equivalent circuits used to fit the experimental impedance data; **(a)** for Pt/C and bare rGO, **(b)** for the three tested catalysts.

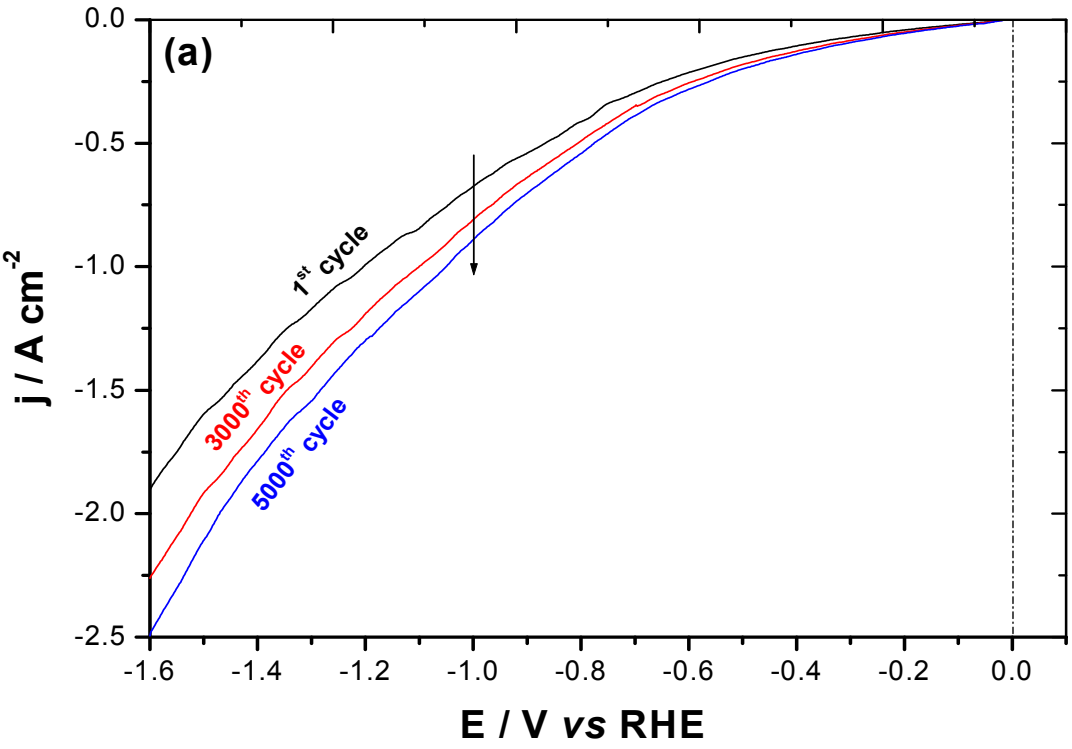

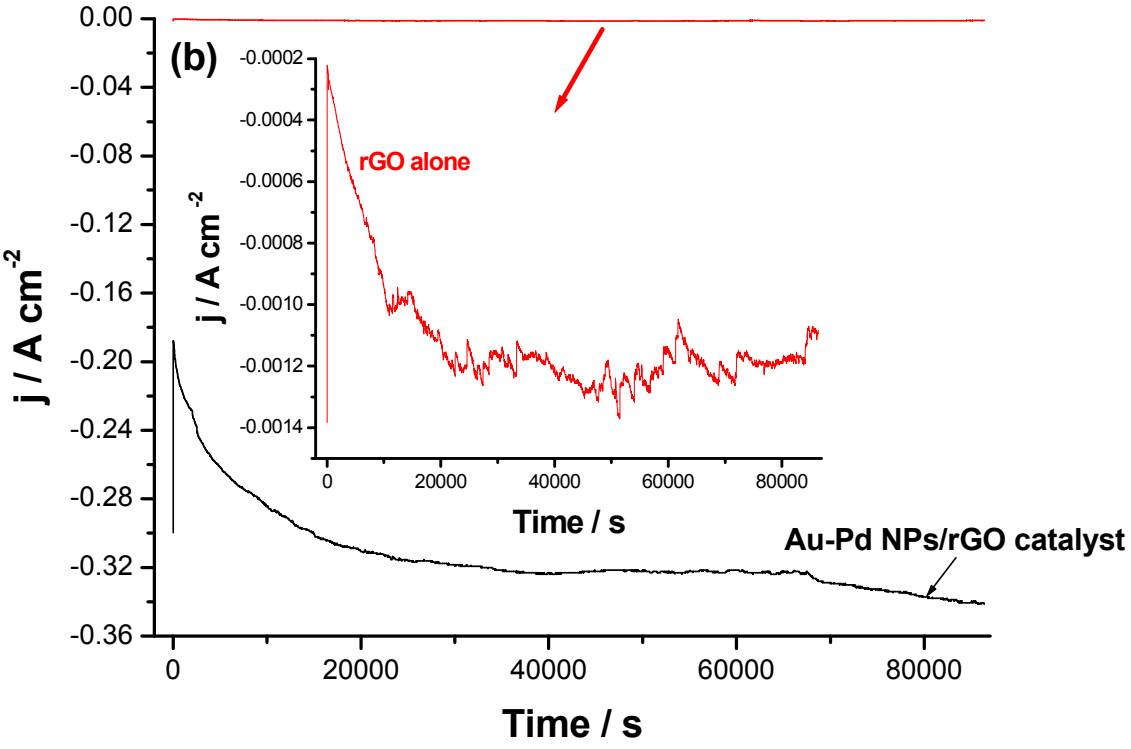

Figure 10: Material stability: (a) Effect of repetitive cycling (5000 cycles) on the electrocatalytic hydrogen evolution of rGO-supported bimetallic Au-Pd NPs (the best catalyst). **(b)** Chronoamperometry measurements (*j vs t*) recorded on the bare rGO and the best catalyst at a constant applied potential of -0.7 V *vs* SCE. All the stability tests were conducted in deaerated H_2SO_4 aqueous solutions (0.5 M) at 25 ^{o}C.

Table 4: Mean value (standard deviation) of the electrochemical impedance parameters recorded for the three tested catalysts in 0.5 M H_2SO_4 solution at a cathodic potential of -0.5 V *vs* SCE at 25 ^oC.

Tested catalyst	R_s Ω cm^2	Q_1 S^n (ω^{-1} cm^{-2})	R_1 Ω cm^2	n_1	C_1 μF cm^{-2}	Q_2 S^n (ω^{-1} cm^{-2})	R_2 Ω cm^2	n_2	C_2 μF cm^{-2}	R_{ct} Ω cm^2
Au NPs/rGO	1.45(0.08)	344.2(3.66)	10.2(0.42)	0.91	196.78(3.1)	72.8(2.18)	48.54(1.27)	0.87	31.31(1.2)	58.74(1.69)
Pd NPs/rGO	1.68(0.11)	739.3(3.59)	22.92(0.63)	0.86	380.65(3.85)	2186.6(5.20)	17.94(0.64)	0.84	1180(4.7)	40.86(1.27)
Au-Pd NPs/rGO	1.26(0.05)	2360.4(1.70)	7.4(0.20)	0.82	970.78(4.92)	9875.6(51.6)	4.8(0.15)	0.80	4608(5.94)	12.2(0.35)

Table 5: Mean value (standard deviation) of the electrochemical impedance parameters recorded for bare rGO and Pt in 0.5 M H_2SO_4 solution at a cathodic potential of -0.5 V *vs* SCE at 25 ^oC.

Tested catalyst	R_s Ω cm^2	Q S^n (ω^{-1} cm^{-2})	R_{ct} Ω cm^2	n	C μF cm^{-2}
bare rGO	1.52(0.1)	3.72(0.105)	2.53(0.11) x 10^6	0.81	6.30(0.28)
Pt	1.97(0.02)	1661.7(1.31)	9.1(0.15)	0.96	1395.4(2.11)